Influence of exchange and correlation on structural and electronic properties of AlN, GaN, and InN polytypes

Luiz Cláudio de Carvalho, André Schleife, and Friedhelm Bechstedt

Phys. Rev. B **84**, 195105 — Published 4 November 2011

DOI: 10.1103/PhysRevB.84.195105

Influence of exchange and correlation on structural and electronic properties of AlN, GaN, and InN polytypes

Luiz Cláudio de Carvalho,[1,2,*] André Schleife,[1,2,3] and Friedhelm Bechstedt[1,2]

[1]*Institut für Festkörpertheorie und -optik, Friedrich-Schiller-Universität, Max-Wien-Platz 1, 07743 Jena, Germany*
[2]*European Theoretical Spectroscopy Facility (ETSF)*
[3]*Condensed Matter and Materials Division, Lawrence Livermore National Laboratory, Livermore, CA 94550, USA*

(Dated: October 19, 2011)

Results for structural and elastic properties of wurtzite and zinc-blende group-III nitrides are calculated using the recently developed AM05 exchange-correlation (XC) functional. They are compared to calculations based on the local-density approximation or the generalized-gradient approximation. We find that AM05 provides a better agreement with experimental results. The atomic geometries are used to compute the quasiparticle band structures within Hedin's *GW* approximation, based on an initial electronic structure calculated using the HSE hybrid XC functional. Important band parameters such as gap energies, crystal-field splittings, spin-orbit coupling constants, and momentum matrix elements are derived. The less precisely known hole masses of InN and the anisotropic spin-orbit constants for wurtzite are predicted. The wave-vector-induced spin-orbit splittings of the valence and conduction bands are discussed.

PACS numbers: 71.15.Mb,71.20.Nr,71.70.Ej

I. INTRODUCTION

Over the last years group III-nitride compounds and their alloys have received a lot of attention because of possible applications in optoelectronic devices that operate in the infrared, visible, and ultraviolet (UV) spectral region. The intense research and the commercial interest in the nitride semiconductors have driven the substantial progress in the knowledge of their properties and the material quality (see e.g. Ref. 1). In particular, remarkable breakthroughs in the growth of InN films by means of molecular beam epitaxy (MBE) have been achieved.[2–4] Surprisingly, for such samples a band edge as low as 0.64 eV was derived from luminescence and optical-absorption measurements,[2–4] which is much smaller than the gap of 1.94 eV obtained in earlier experiments.[5] Hence, by alloying AlN, GaN and InN, it is possible to tune the band gap over a wide spectral range reaching from 0.64 eV up to 6.2 eV, i.e., covering the entire solar spectrum.[6] In addition, free-electron concentrations smaller than 10^{18} cm^{-3} and electron mobilities larger than 2000 cm^2/Vs were achieved.[7] Besides the fundamental gap also the band dispersion and especially the electron mass can be varied over a wide range.[1] The tuning possibilities provide some interesting applications of the nitrides and their alloys in (i) solar cells,[6] (ii) light-emitting and laser diodes operating in the blue and UV spectral range,[8,9] (iii) chemical sensors,[10] and (iv) electronic devices operating under extreme conditions or even for quantum cryptography applications.[11]

The three group-III nitrides AlN, GaN, and InN crystallize in the wurtzite (*wz*) structure under ambient conditions, which corresponds to the P6$_3$mc (C_{6v}^4) space group for vanishing strain in the samples. The group III-nitrides can also be grown in the cubic zinc-blende (*zb*) structure with space group $F\overline{4}3m$ (T_d^2) by means of different epitaxy techniques such as MBE.[12] However, even though high-quality films of AlN, GaN and InN have been synthesized, research and applications were limited since large single crystals cannot be grown. Therefore, existing experimental studies are usually restricted to investigations of epitaxial layers and, hence, may be influenced by the respective substrate, the interfaces, and spontaneous as well as piezoelectric fields. Correspondingly, a large variety of experimental results exists. For instance, the electronic band parameters such as fundamental gaps, effective electron masses, and valence band (VB) dispersions (as well as their variation with strain) are less precisely known for the bulk materials. One prominent example is the recent discovery of the InN gap smaller than 0.7 eV.[2,4]

Parameter-free calculations are a promising complement to experiment, since they are not only capable of providing material parameters but also give valuable insights into the underlying physics. *Ab-initio* studies allow the investigation of arbitrary crystal structures and, hence, can help to understand the *wz* and *zb* polytypes of the nitrides including the influence of the actual atomic geometry on the material parameters. Remarkable progress in the determination of band gaps, effective masses, and $\mathbf{k}\cdot\mathbf{p}$ parameters has been made recently for the nitrides by applying modern quasiparticle electronic-structure theory (based on the OEPx+G_0W_0 approach[13] or the self-consistent *GW* method[14]). However, these calculations were restricted to lattice constants[13] or unit-cell volumes[14] obtained in experiments. In both papers the hole effective masses of InN have not been computed and the spin-orbit coupling (SOC) has not been taken into account neither for the *wz* nor the *zb* polytype. However, such calculations are now possible. For different group-II oxides the influence of SOC has been successfully included in calculations of the electronic structure and proven to be important.[15–18]

In this paper, the consequences for the quasiparticle (QP) electronic structures upon inclusion of the SOC are investigated for the *wz* and *zb* polytypes of the group-III nitrides AlN, GaN, and InN. Lattice parameters as obtained from three different approximations to exchange and correlation (XC) within density functional theory (DFT) are employed. In Sec. II, the theoretical framework and its numerical implementation are briefly presented. The results for the energetic, structural, and elastic properties are compared in Sec. III. The QP band structures and band structure parameters computed within the *GW* approximation based on an electronic structure obtained using a hybrid XC functional are discussed in the light of recent experimental data in Sec. IV. The effect of the SOC is studied on band splittings and band dispersions. Section V gives a brief summary and concludes the paper.

II. THEORETICAL FRAMEWORK AND COMPUTATIONAL DETAILS

A. Ground-state properties

Ground-state properties such as the structural and elastic properties can be derived from total-energy minimizations within DFT.[19,20] The XC functional is not exactly known and approximations have to be used. Both the local density approximation (LDA) and the semi-local generalized-gradient approximation (GGA) are common,[20] however, the XC choice affects the total energy and consequently the atomic geometry of the system. It has been found that the LDA tends to an overbinding, i.e., leading to lattice constants that are $\approx 1\,\%$ smaller than found in experiment, whereas commonly used GGA functionals underestimate the binding and yield too large lattice constants (by up to 2 %) as demonstrated below.

In contrast, the recently developed AM05 XC functional[21] seems to overcome some of the shortcomings related to earlier versions of the GGA. It has been designed to treat systems with varying electron densities (for instance systems that are composed of bulk- and surface-like regions) by exploiting the subsystem functional scheme.[22] For each region, a different XC subsystem functional is created, and the functionals are joined by interpolation based on an index.[21] Mattsson *et al.* compared the

lattice parameters obtained using AM05 for a large set of crystalline solids to the ones calculated via the LDA and other GGA XC functionals. They found that AM05 systematically performs better with an accuracy almost as good as advanced hybrid functionals.[23]

In this work, the parameters a, c, and u of the *wz* lattice and the cubic a_0 of the *zb* lattice are computed by minimizing the total energy E_{tot} with respect to the atomic coordinates. It has been ensured that the Hellmann-Feynman forces on the atoms are smaller than 1 meV/Å. Moreover, the isothermal bulk modulus B_0 as well as its pressure derivative B_0' follow from a fit of $E_{\mathrm{tot}}(V)$ to the Murnaghan equation of state;[24] V denotes the volume of the cells. In order to study the influence of the XC functional, the LDA as parametrized by Perdew and Zunger[25] is used, as well as the PBE-GGA described by Perdew, Burke, and Ernzerhof.[26] In addition, the AM05 XC functional[21] is used to partly account for the inhomogeneity of the electron gas.

All DFT calculations are performed within the implementation in the Vienna *Ab-Initio* Simulation Package (VASP).[27,28] The pseudopotentials are generated by means of the projector-augmented-wave method.[29] Thereby, the N 2*s*, N 2*p*, In 4*d*, In 5*s*, In 5*p*, Ga 3*d*, Ga 4*s*, Ga 4*p*, Al 3*s*, and the Al 3*p* electrons are included in the valence shell. As suggested in Ref. 23, the PBE PAW pseudopotentials were used for the AM05 calculations. In the region between the atomic cores the wave functions are expanded into plane waves up to a cutoff energy of 400 eV. The Brillouin zone (BZ) is sampled using $8 \times 8 \times 8$ ($8 \times 8 \times 6$) Monkhorst-Pack[30] **k**-points for *zb*-AlN (*wz*-AlN) and $16 \times 16 \times 16$ ($16 \times 16 \times 12$) meshes for *zb*-GaN and *zb*-InN (*wz*-GaN and *wz*-InN).

B. Single-particle excitations

The solution of the Kohn-Sham (KS) equation[20] of DFT provides the true ground-state electron density of the interacting electrons as well as eigenvalues and eigenstates of non-interacting KS particles. However, experimental techniques such as photoelectron emission, inverse photoelectron spectroscopy, or tunnel spectroscopy, that measure band structures or densities of states (DOS), involve electronic excitations and rather probe single-QP energies. Also in transport experiments, phenomena of charged carriers (electrons or holes) and, therefore, electronic excitation effects, play a role.

DFT, however, suffers from the so-called band-gap problem: The KS gaps calculated for semiconductors and insulators significantly underestimate the QP gaps derived from measurements.[31] The band-gap problem can be solved within the framework of the many-body perturbation theory,[32] which yields a QP equation[31] that properly includes the XC self-energy of the electrons and, hence, accounts for the excitation aspect. The non-Hermitian, non-local, and energy-dependent self-energy is usually described by means of Hedin's *GW* approximation,[33,34] where G denotes the single-particle Green's function and W represents the dynamically screened Coulomb interaction.

Usually it is sufficient to treat the self-energy effects within first-order-perturbation theory.[35] This approach of calculating QP eigenvalues $\varepsilon_{\nu}^{\mathrm{QP}}(\mathbf{k})$, where ν is the band index and $\mathbf{k}$ the Bloch wave vector in the BZ, is called G_0W_0 and is also implemented in the VASP code.[36] For relatively homogeneous electronic systems the G_0W_0 corrections to the KS eigenvalues from DFT-LDA or DFT-GGA lead to electronic band structures that are in reasonable agreement with measurements.[31]

However, for compounds with first-row elements, such as the nitrides, the LDA/GGA+G_0W_0 procedure still underestimates the band gaps.[37] The idea of an iterative solution of the QP equation seems to be more promising,[35,38] unfortunately it is inherently linked to a much higher computational cost. Therefore, computing the QP energies from one step of perturbation theory, based on an initial electronic structure that is closer to the final self-consistent solution than the KS eigenvalues and eigenstates are, is an efficient alternative. Such an improved starting point can be obtained from the exact-exchange optimized-effective potential (OEPx) approach[39] or by solving a generalized KS equation with a spatially non-local XC potential.[37,40]

The HSE hybrid functional by Heyd, Scuseria, and Ernzerhof[41,42] (based on HSE06,[43] but using a range parameter of $\omega = 0.15$ a.u.$^{-1}$ instead of $\omega = 0.11$ a.u.$^{-1}$, see disambiguation in Ref. 44), which has proven to work well for InN polytypes,[37,45] combines one quarter ($\alpha = 0.25$) of the non-local Hartree-Fock exchange with three quarters of the local exchange obtained using the PBE-GGA functional. Therefore, it effectively simulates the screened-exchange contribution to the *GW* self-energy. The inverse of the prefactor α of the Fock operator can be interpreted as static screening corresponding to a dielectric constant of 4. Moreover, the parameter ω describes the separation of the Coulomb potential into a short- and a long-range part. The latter is assumed to be screened in a Thomas-Fermi-like manner in solids, due to the total valence electron gas.

In this work, SOC is taken into account via a non-collinear description[46] within the calculation of the HSE electronic structure.[15–17] It is not just numerically very expensive to employ a full HSE+*GW* approach including non-collinear spins, moreover, the replacement of wave functions by spinors is not enough because of the coupling of orbital and spin motion. Hence, since the spin is not conserved,[47] a simple generalization of the available codes is difficult. However, since all orbital contributions to the mixed states are mostly *p*-like the same influence of the QP corrections can be expected for the spin-orbit-split band energies at a given Bloch wave vector. Consequently, the SOC should be almost uninfluenced by the QP effects. This especially holds for HSE values close to the QP ones. The accuracy of this efficient approximation has been demonstrated for group-II monoxides.[15–17]

Even though results for the lattice parameters obtained from HSE calculations seem to be in better agreement with experimental values than results of LDA and GGA studies,[48] in this work it is strictly distinguished between ground- and excited-state

properties. Hence, atomic geometries are only computed based on the LDA, the PBE-GGA, and the AM05 XC functionals, while the QP calculations follow the HSE+G_0W_0+SOC approximation.

III. ENERGETIC, STRUCTURAL AND ELASTIC PARAMETERS

The lattice parameters a_0 (for *zb* polytype) as well as a, c, u, and c/a (for *wz* polytype) as derived from the DFT calculations (cf. Sec. II A) are reported along with the bulk moduli B_0 and their pressure derivatives B_0' in Table I. From comparison to experimental values[49–51,53,54] it is confirmed that the LDA leads to an overbinding for the group-III nitrides; the optimized lattice constants are smaller than the measured values. In contrast, the lattice parameters turn out to be larger when the PBE-GGA is used to describe XC, which corresponds to the underbinding mentioned before.

Interestingly, the AM05 functional indeed yields lattice constants in close agreement to experiment[49,51,53] for AlN and GaN polytypes. The small overestimation of $< 0.6\,\%$ for the a_0, a, and c lattice constants obtained for InN using the AM05 functional can be a consequence of the fact that the layers used in the measurements might not be completely unstrained, defect-free, and polytype-pure. The excellent agreement of the AM05 lattice constants with measured values for AlN and GaN leads us to believe that this functional also gives reliable lattice constants for InN.

In contrast to what is observed for the lattice constants a and c of the *wz* crystals, the c/a ratio and the u parameter are rather independent of the description of XC (cf. Table I). There are only very small changes along the functionals LDA, AM05, and PBE-GGA. Along the row *wz*-AlN, *wz*-GaN, and *wz*-InN u takes a less pronounced minimum for GaN. The experimental u parameter decreases monotonously towards the ideal tetrahedron value of $u = 0.375$, in agreement with the fact that this parameter is almost indirectly proportional to the bond ionicities $g = 0.794$ (AlN), 0.780 (GaN), and 0.853 (InN).[55] The non-monotonous behavior of the c/a ratio for both computed and measured values when going from AlN over GaN to InN is because GaN and InN (as opposed to AlN) have shallow d electrons. The values remain below the ideal ratio $c/a = 1.633$ in agreement with the theoretical prediction[56] that for $c/a < 1.633$ a compound crystallizes in *wz* structure under ambient conditions. A similar non-monotonous behavior is observed for the stability of the polytypes as described by the total energy differences between *zb* and *wz*, $\Delta E_{\rm tot} = E_{\rm tot}(zb) - E_{\rm tot}(wz)$. The $\Delta E_{\rm tot}$ (cf. Table I) exhibit a minimum for GaN, indicating that *zb*-GaN most likely can be grown not too far from equilibrium, whereas that would be more difficult for AlN and InN from an energetical point of view. The $\Delta E_{\rm tot}$ in Table I are in rough agreement with values obtained from DFT-LDA.[56]

The pair volumes $\Omega^{zb}_{\rm pair} = 1/4\ a_0^3$ and $\Omega^{wz}_{\rm pair} = \sqrt{3}/4\ a^2 c$, that are occupied by one cation-anion pair, are practically the same for the *zb* or *wz* polytypes of each material. In addition, it is found that they increase along the row AlN, GaN, InN (for instance $\Omega^{zb}_{\rm pair}$=20.9, 22.7, and 31.3 Å^3 as derived using the AM05 functional), which matches the trend of an increasing sum of the covalent radii of the anion and the cation: 1.93, 2.01 and 2.19 Å.[57] Moreover, due to the aforementioned overbinding, the volumes of the unit cells calculated using the LDA are smaller than the ones obtained with the AM05 functional. The PBE-GGA leads to the largest unit-cell volumes, which is in agreement with the underbinding mentioned above.

The inverse compressibility B_0 increases along the row InN, GaN, and AlN when the same XC functional is used. B_0 of one and the same material also increases when going from PBE-GGA over AM05 to LDA (cf. Table I). Furthermore, there is an influence of the polytype on B_0: In the case of AlN the values for *zb* are larger than the *wz* ones, while the opposite is true for GaN and InN. This seems again to be a consequence of the contributions of the Ga 3*d* or In 4*d* electrons, respectively, to the chemical bonding. Comparing the calculated B_0 to experimental values[52,54] shows that the agreement is quite good for the *zb* polymorphs when AM05 is used. For the *wz* polymorphs of GaN and InN the measured values are in between the PBE-GGA and AM05 ones. The pressure coefficients B_0' vary between $3-5$ and no clear trend for different XC functionals or materials is spotted. The large value of $B_0' = 12.7$ measured[54] for *wz*-InN arises probably due to sample-quality issues.

IV. QUASIPARTICLE ELECTRONIC STRUCTURE

In Sec. III it has been shown that the atomic geometries obtained using the AM05 XC functional agree better with measured results than the LDA or PBE-GGA ones. Hence, only results for the electronic QP energies based on the AM05 geometries are presented. In Ref. 58 (Ref. 59) the HSE+G_0W_0 approach has been applied to the DFT-LDA geometries of InN (AlN). As indicated in the text, the LDA or PBE-GGA geometries are used to study atomic structures that are hydrostatically strained with respect to the AM05 equilibrium geometries. In these cases the indirect influence of the XC functional used in the ground-state studies within DFT on the electronic structure (via the atomic geometry) and the direct influence of XC according to the GW self-energy are discussed together.

A. Band structures

The QP band structures of AlN, GaN, and InN calculated for the *zb* (*wz*) AM05 atomic geometries are shown along with the corresponding DOS in Fig. 1 (Fig. 2). Since the spin-orbit splittings are small, they are not shown in these figures and the notations of the irreducible representations are given accordingly.[60–62] All band structures show a pronounced minimum of the lowest conduction band (CB) near the BZ center Γ. The dispersion of this band around Γ increases along the row AlN, GaN and InN, thereby closing the fundamental energy gap. This can be explained by the In 5*s* and Ga 4*s* levels being lower in energy than the Al 3*s* one[63] and the reduction of the interatomic interaction along the row AlN, GaN, and InN.[64] The strong CB dispersion is also visible by the low state density in the lowest part of the empty DOS (see Figs. 1 and 2). Another reason that the gaps of InN and GaN are much smaller than the one of AlN is the remarkable *pd* hybridization in both materials.[65] This effect causes a strong *pd* repulsion at Γ which is not present for AlN and hence renders *zb*-AlN an indirect semiconductor with a CB minimum situated at the *X* point.

As can be seen in Figs. 1 and 2, the *d* electrons also influence the VB structure. More specifically, it is observed that the ionic gap between the uppermost three (twofold spin degenerate) *p*-like VBs and the lowest (twofold spin degenerate) *s*-like VB does not follow the trend of the charge asymmetry coefficients.[55] The reason for this behavior is the energetic overlap of the N 2*s* states and the Ga 3*d* or In 4*d* states, respectively, the so-called *sd* hybridization. This effect is symmetry-forbidden at Γ,[66] however, for *zb*-GaN and *zb*-InN it leads to a splitting into a lower and an upper split-off band for all **k**-points away from the BZ center. In addition, four dispersionless low-lying bands appear at −16 eV (GaN) or −15 eV (InN). All these bands give rise to pronounced peaks in the DOS which are clearly visible in photoemission experiments.[67]

B. Fundamental gaps and their volume/pressure dependence

The fundamental gaps at the Γ point of the BZ for AlN, GaN, and InN in the *zb* and the *wz* structure are summarized in Table II. They separate CB states of Γ_{1c} type from VB states of Γ_{15v} type for the *zb* crystals as well as Γ_{1c}-like CB states from Γ_{5v}-like (*wz*-GaN, *wz*-InN) or Γ_{1v}-like (*wz*-AlN) VB states. Here, the denotation is changed back from Fig. 2 (Γ_6 Rashba notation[62]) to the textbook version (Γ_5 Ref. 60). In addition, also the indirect fundamental gap of *zb*-AlN between X_{1c}-like and Γ_{15v}-like states is given in Table II. These results clearly demonstrate that the approach applied in this work, i.e., calculating QP energies within the *GW* approximation based on an initial electronic structure from HSE, gives excellent fundamental gaps for the nitrides. While this is true for the atomic geometries obtained using the AM05 XC functional, the ones calculated based on the LDA (PBE-GGA) lead to an overestimation (underestimation) of the direct gaps in comparison to measured values. Thereby, it is found that the relative variation of the gap with the cell volume is most drastic for InN, while the influence on the indirect gap of *zb*-AlN is much weaker. This is a consequence of the opposite shifts of the Γ_{1c} and X_{1c} levels in *zb*-AlN when the volume changes.

Using the changes of the unit-cell volume due to the different XC functionals (cf. Table I) and the fundamental band gaps, the hydrostatic band-gap deformation potentials $\alpha_V = \delta E_g / \delta \ln V$ are derived (cf. Table II). They are slightly larger than values from an equally sophisticated QP approach.[13] The hydrostatic pressure coefficients $\alpha_p = -\alpha_V / B_0$ follow with the bulk moduli in Table I. The results for α_V and α_p are in excellent agreement with measured values (see e.g. collection in Ref. 13).

In Table III the fundamental band gaps of the *zb* mononitrides are given as calculated based on the different equilibrium geometries (cf. Table I) and using different levels of approximation for the XC self-energy. These numbers confirm that the KS eigenvalues obtained using a local/semi-local XC functional are smaller compared to the more sophisticated approximations. InN even turns out to be a zero-gap semiconductor in these cases since the ordering of the Γ_{1c} and the Γ_{15v} levels is inverted.[71] Including the screened-exchange contribution[34] by using the spatially non-local HSE functional shifts the electron and hole eigenvalues in opposite directions.[31] Consequently, the gaps are by about 1 eV (AlN, GaN) or 0.3 eV (InN) larger than the KS gaps (cf. Table III). In a next step, the correct screening (including its dynamics) as well as the Coulomb hole contribution[34] are taken into account by calculating QP energies within the G_0W_0 approximation. This leads to an additional increase of the gaps by about 0.9 eV (AlN), 0.6 eV (GaN), and 0.1 eV (InN), which corresponds to roughly 20 % of the true fundamental gap. Therefore, we find that eigenvalues obtained in an HSE calculation significantly improve over the DFT-LDA/DFT-GGA ones. However, only the full XC self-energy (as approximately calculated within the G_0W_0 approach) leads to QP gaps that are in good agreement with measured values.

C. Valence-band splittings

Without SOC the VB maximum of the *zb* nitrides is a threefold degenerate state with Γ_{15v} symmetry which splits into a Γ_{8v} (fourfold degenerate) and a Γ_{6v} (twofold degenerate) level in the presence of the spin-orbit interaction.[60] The corresponding $\Delta_{so} = \varepsilon(\Gamma_{8v}) - \varepsilon(\Gamma_{6v})$ are compiled in Table IV. These numbers show that the choice of the XC functional indirectly influences the splittings via the atomic geometry. However, there is no clear trend with the (overestimated or underestimated) lattice

constants, since also the mixing of the p and d like levels changes and, hence, affects the SOC splitting (see below). Moreover, the values for Δ_{so} do not vary strongly for the different cubic group-III nitrides. The results in Table IV agree well with values from previous DFT-LDA calculations[72] from which 20.0, 18.5, and 12.6 meV was derived for AlN, GaN, and InN, respectively. Also the values $\Delta_{so} = 19$, 17, and 5 meV which have been recommended by Vurgaftman and Meyer[1] are very close.

In the case of GaN and InN the Δ_{so} are so small compared to AlN since the atomic spin-orbit splittings[73] for the Ga $4p$ (98 meV) and Ga $3d$ (537 meV) electrons or the In $5p$ (264 meV) and In $4d$ (958 meV) states, respectively, partially compensate each other. This compensation arises due to the pd hybridization of atomic-like p and d states and leads to the values given in Table IV. Interestingly, for GaN and InN the spin-orbit splittings between $L_{4,5}$ and L_6 states, $\Delta_{so}(L)$, are larger than the respective splittings at the Γ point. In contrast to AlN, the rule[72] $\Delta_{so}(L)/\Delta_{so}(\Gamma) = 2/3$ is violated for GaN and InN. A similar effect has been observed for other tetrahedrally coordinated III-V compounds with relatively large differences of the covalent radii, for instance InP.[74]

For *wz* crystals the VB structure is more complex due to the hexagonal crystal field which leads to a crystal-field splitting. Hence, without SOC one finds the twofold degenerate Γ_{5v} and the non-degenerate Γ_{1v} states at the VB maximum. Thereby, we use the Bouckaert, Smoluchowski and Wigner notation[60,61] Γ_{15v} which leads to Γ_{5v} and Γ_{1v} instead of Γ_{6v} and Γ_{1v} as in the Rashba denotation[62] applied in Fig. 2. The Γ_{5v} state splits into Γ_{9v} and Γ_{7v} levels and Γ_{1v} becomes a level with Γ_{7v} symmetry in the presence of SOC.

The values for the crystal-field splittings Δ_{cf} in Table IV indicate a small influence of the *GW* corrections on the crystal-field splittings: the QP shifts towards lower band energies are larger for the Γ_{5v} states than for the Γ_{1v} states. Consequently, the QP corrections reduce the crystal-field splitting for *wz*-GaN and *wz*-InN by about 3 – 7 meV. In the case of *wz*-AlN an enlargement of the absolute value by about 17 – 20 meV is computed due to the negative sign of Δ_{cf}. The absolute splittings in Table IV are somewhat larger than the values recommended by Vurgaftman and Meyer.[1] However, the sign and, hence, the ordering of the Γ_{5v} and Γ_{1v} states are the same. Moreover, the values calculated in this work are in good agreement with other *ab-initio* calculations, e.g. collection in Ref. 63 and references therein. The QP calculations in Ref. 13 tend to overestimate the absolute values for Δ_{cf}^0.

Within $\mathbf{k}\cdot\mathbf{p}$ theory the energy differences of the uppermost valence levels in a *wz* crystal, $\Delta E_1 = \varepsilon(\Gamma_{9v}) - \varepsilon(\Gamma_{7+v})$ and $\Delta E_2 = \varepsilon(\Gamma_{9v}) - \varepsilon(\Gamma_{7-v})$, can be described by[75]

$$\begin{aligned}\Delta E_{1/2} &= \varepsilon\left(\Gamma_{9v}\right) - \varepsilon\left(\Gamma_{7+/-v}\right) \\ &= \frac{1}{2}\left(\Delta_{cf} + \Delta_{so\|}\right) \mp \frac{1}{2}\sqrt{\left(\Delta_{cf} - \frac{1}{3}\Delta_{so\|}\right)^2 + \frac{8}{9}\Delta_{so\perp}^2}.\end{aligned} \tag{1}$$

In Eq. (1), $3i\Delta_{so\|} = \langle y|H_{sz}|x\rangle$ and $3i\Delta_{so\perp} = \langle z|H_{sx}|y\rangle = -\langle z|H_{sy}|x\rangle$ are the spin-orbit splitting parameters; the spin-orbit interaction H_{so} is divided according to $H_{so} = H_{sx}\sigma_x + H_{sy}\sigma_y + H_{sz}\sigma_z$ by means of the Pauli spin matrices σ. Therein, $|x\rangle$, $|y\rangle$, and $|z\rangle$ describe the p like basis functions at Γ. In addition, Δ_{cf} represents the differences in the VB eigenvalues of the $|x\rangle$ ($|y\rangle$) and the $|z\rangle$ states.

However, Eq. (1) indicates a complication for both theory as well as experiment. In band-structure calculations and also in all spectroscopies only energy differences such as ΔE_1 and ΔE_2 are determined. Hence, only two numbers are available to determine the three band-structure parameters Δ_{cf}, $\Delta_{so\|}$, and $\Delta_{so\perp}$ from Eq. (1). If no additional assumption is made, the lack of one parameter for the determination of Δ_{cf}, $\Delta_{so\|}$, and $\Delta_{so\perp}$ leads to a parameter field $\Delta_{so\|} = \Delta_{so\|}(\Delta_{cf})$ and $\Delta_{so\perp} = \Delta_{so\perp}(\Delta_{cf})$ which is visualized in Fig. 3. One possible additional assumption to fix all parameters is the quasicubic approximation $\Delta_{so\|} = \Delta_{so\perp} = \Delta_{so}^{qc}$ and $\Delta_{cf} = \Delta_{cf}^{qc}$. Interestingly, when $\Delta_{cf} > 0$ (as found for GaN and InN) the resulting Δ_{cf}^{qc} are not very different from the values computed in the absence of SOC (cf. Table IV). For $\Delta_{cf} < 0$ (AlN) a further increase of the absolute values is observed. In any case the quasicubic spin-orbit splitting constant Δ_{so}^{qc} is by nearly a factor of 2 (1.5) smaller than its *zb* value for InN (GaN), while there is no such deviation for AlN, which has no d electrons. This has recently been discussed for the first time,[45] and, according to the results of the present work, the recommendation[1] to choose the same spin-orbit splittings for *wz* and *zb* fails for compounds with shallow d electrons. Another additional assumption can be derived by identifying $\Delta_{cf} = \Delta_{cf}^0$ which leads to $\Delta_{so\|} \neq \Delta_{so\perp}$. Moreover, the ΔE_1 and ΔE_2 values in Table IV indicate that Δ_{cf}, as computed using the eigenvalues without SOC, is almost in agreement with the average distance $\frac{1}{2}[\varepsilon(\Gamma_{9v}) + \varepsilon(\Gamma_{7+v}) - \varepsilon(\Gamma_{7-v})] = \frac{1}{2}[\Delta E_1 + \Delta E_2]$ between the valence levels including SOC. Therefore, the choice $\Delta_{cf} = \Delta_{cf}^0$ seems to be reasonable. For a more detailed comparison of theoretical and experimental values, the reader is referred to Ref. 45.

D. Band dispersion

In Fig. 4 the large impact of the spin-orbit and crystal-field splittings on the dispersion of the uppermost valence bands around Γ is shown for the $\Gamma - X$ and the $\Gamma - L$ directions in the fcc BZ as well as the $\Gamma - A$ and the $\Gamma - M$ directions in the hexagonal BZ. Figure 4a illustrates the splittings of the six uppermost VBs of the *zb* polymorphs: while the degeneracy of the heavy-hole (hh)

bands, which belong to the Λ_4 and Λ_5 irreducible representations, is lifted along the $\Gamma-L$ direction, the light hole (lh) and the spin-orbit split-off (so) bands remain twofold degenerate.

The degeneracy of the L_4 and L_5 representations occurs due to the time-reversal symmetry. These effects are well known for other *zb* crystals[74,76,77] as well as for the nitrides.[72] The splitting of the hh bands near Γ along the [111] direction can be described by the relation[74] $\Delta E_{\rm hh} = -2\sqrt{2}C_k \cdot k$. Using our *ab-initio* results we derive values of $C_k = -0.005$, -0.063 and -0.178 eVÅ for AlN, GaN and InN which are in qualitative agreement with the trends found for group-V compounds containing Al, Ga, and In.[74] The strong increase of the C_k going from AlN to GaN or InN can be traced back to the presence of the shallow *d* states that contribute to the top of the VBs in GaN and InN.[72,78]

Figure 4b illustrates the splitting effects for the VBs of the *wz* nitrides along the $\Gamma-M$ direction in the BZ. In this case all the irreducible representations compatible with spin are singly degenerate (except for the BZ center and the BZ boundary). In contrast to that, no spin splitting of the three VBs appears along the hexagonal $\Gamma-A$ direction since the small point group of these **k** points is C_{6v}. Hence, the irreducible representations that are compatible with spin are twofold degenerate like Γ_9, Γ_{7+} and Γ_{7-} in the BZ center.[79] Indeed, for GaN and InN a clear splitting of the lh bands is visible in Fig. 4b, whereas the splittings for the other bands are small.

However, as can be seen for *wz*-GaN and *wz*-InN in Fig. 4b, the interpretation of the VBs can be more complex due to state mixing and band crossings near the Γ point. For these materials the definition of spin splittings that are linear in the **k** vector is impossible. For that reason the spin-orbit splittings of the hh, lh, and ch bands along the $\Gamma-M$ direction are compared to the corresponding splitting of the lowest CB in Fig. 5. This shows that the influence of the SOC on the hh band and the lowest CB remains relatively small. Contrary, the impact on the lh and the ch bands is much larger. As observed for the *zb* polymorphs, there is a clear chemical trend of increasing SOC splittings along the row AlN, GaN, and InN. For InN the **k**-vector-induced splittings even approach the order of magnitude of $\Delta_{\rm so}$ (cf. Table IV). The non-monotonous behavior of the wave-vector-induced splittings of the lh and ch bands of *wz*-GaN and *wz*-InN is a consequence of the corresponding band crossings along $\Gamma-M$ in Fig. 4b.

E. Effective masses

The band dispersions and curvatures away from Γ in Fig. 4 depend not only on the splittings of the valence states but also on the coupling between the lowest CB and the uppermost VBs. Within $\mathbf{k}\cdot\mathbf{p}$ theory[60,75] this coupling is governed by the interaction of the *s*-like CB state $|s\rangle$ and the *p*-like valence wave functions $|x\rangle$, $|y\rangle$, $|z\rangle$ at Γ, mediated by the momentum operator $\mathbf{p}$. The respective matrix elements $\mathrm{P}_\perp = \frac{\hbar}{2m_0}\langle s|\mathbf{p}_x|x\rangle = \frac{\hbar}{2m_0}\langle s|\mathbf{p}_y|y\rangle$ or $\mathrm{P}_\parallel = \frac{\hbar}{2m_0}\langle s|\mathbf{p}_z|z\rangle$ give rise to relatively large values. In units of energy, the Kane parameters $E_{p\perp/\parallel} = \frac{2m_0}{\hbar^2}\mathrm{P}^2_{\perp/\parallel}$ calculated using the HSE wave functions are $E_p = 15.86\,/\,13.26\,/\,9.50$ eV for *zb*-AlN / *zb*-GaN / *zb*-InN or $E_{p\perp} = 15.78\,/\,12.83\,/\,9.39$ eV and $E_{p\parallel} = 15.92\,/\,14.79\,/\,10.52$ eV in the *wz* case. These values are close to those derived from experimental data for InN[80,81] but seem to underestimate the values suggested for GaN.[82,83] The agreement with theoretical values[13] calculated from the OEPx wave functions is good. However, the agreement is worse when comparing to results for GaN that take the *GW* corrections into account.[14]

The effective electron and hole masses are extracted from the HSE band-structure calculations (including spin-orbit interaction), assuming that the influence of the QP corrections on the band dispersion is small. Thereby, the complex curvature of the VBs shown in Fig. 4 renders the determination of the effective masses difficult. To avoid these complications, the lifting of degeneracies of the lh and the hh bands occurring away from the Γ point due to SOC are neglected by using averages over the **k**-vector-induced spin-orbit-split band pairs.

In addition, it is essential to employ only the close proximity of Γ for the determination of the effective masses. The use of a larger **k**-point region would give rise to larger effective masses of the lh band otherwise due to the significant non-parabolicity of the corresponding bands (cf. Fig. 4a). However, the strong warping of the hh and the lh bands observed for the *zb* polymorphs is taken into account. In the *wz* case only wave vectors that are closer to the Γ point than the band-crossing points are taken into consideration. Figure 4b shows that especially the lh masses along the $\Gamma-M$ direction may sensitively depend on the wave-vector range chosen for their determination. This is not merely a shortcoming of the theoretical description but also holds for their experimental determination by varying the hole concentrations. For the electron masses the situation is less complex as illustrated by the band structures in Figs. 1 and 2.

The effective masses of the uppermost three VBs and the lowest CB are given for the *zb* polytypes in Table V. While the HSE+SOC results describe the electron masses for *zb*-GaN quite well, they slightly overestimate them for *zb*-InN in comparison to measured values. Nevertheless, the numbers given in Table V confirm the extremely small electron mass for InN found in experiments. Overall, the results in the present work are closer to experimentally determined masses than found in previous calculations.[85,87] The values of $m_{\mathrm{e}\perp}(X) = 0.30\,m_0$ and $m_{\mathrm{e}\parallel}(X) = 0.53\,m_0$ calculated for the CB minimum of *zb*-AlN in this work agree well with $m_{\mathrm{e}\perp}(X) = 0.33\,m_0$ and $m_{\mathrm{e}\parallel}(X) = 0.52\,m_0$ as derived within the LDA using the experimental lattice parameters.[86] The same holds for the effective masses of AlN and GaN at the CB minimum at the Γ point.[86] Especially for AlN and GaN the hole masses agree very well with the fully relativistic LDA calculations of Ramos *et al.*,[84] as well as with other first-principles

calculations based on local or semilocal XC functionals,[86] empirical-pseudopotentials[85] or the OEPx+G_0W_0 approach.[13] In general and also in our studies, no clear trend of the hole masses with the different XC functionals is found.

The electron masses at the Γ point decrease along the row AlN, GaN, and InN. Qualitatively they nearly agree with the values of 0.29, 0.20, and 0.04 obtained using the relation $m_e(\Gamma)/m_0 = 1/[1+E_p/E_g]$. The hole masses of the spin-orbit split-off VBs in Table V are isotropic and also decrease from AlN over GaN to InN. The values in Table V show that the masses of the lh band are by a factor of $m_{hh}/m_{lh} = 3-27$ lighter than the hh ones. The masses of the lh bands approach values on the order of the electron effective mass. The fact that the hh and the lh masses (Table V) are different in the three directions confirms the well-known warped isoenergy surfaces of the Kane model.[60]

The six different hh and lh masses given in Table V contain more information than is included in the Kane model of the three uppermost VBs. In the Kane model these bands are characterized by three Luttinger parameters γ_1, γ_2, and γ_3.[82,86] Using the HSE+SOC values, we determine the Luttinger parameters along the $\Gamma-X$ and the $\Gamma-L$ directions using the assumptions $\gamma_1 = \frac{m_0}{4}(1/m_{hh}^{[111]} + 1/m_{lh}^{[111]} + 1/m_{hh}^{[001]} + 1/m_{lh}^{[001]})$, $\gamma_2 = \frac{m_0}{4}(1/m_{lh}^{[001]} - 1/m_{hh}^{[001]})$, and $\gamma_3 = \frac{m_0}{4}(1/m_{lh}^{[111]} - 1/m_{hh}^{[111]})$. Using the masses given in Table V we obtain $\gamma_1 = 1.478/2.409/7.143$, $\gamma_2 = 0.379/0.592/2.890$, and $\gamma_3 = 0.595/0.959/3.439$ for AlN / GaN / InN. We find a dramatic increase of the Luttinger parameters from AlN via GaN to InN. The present results are close to the results of an OEPx+G_0W_0 calculation (neglecting SOC).[13] However, for InN we obtain somewhat larger Luttinger parameters.

In the case of the *wz* polymorphs the band anisotropy is influenced by the lower crystal symmetry. The uppermost VBs are isotropic in the plane perpendicular to the *c*-axis due to the lift of the degeneracy at Γ. Therefore, the curvatures of the bands along the $\Gamma-M$ and the $\Gamma-K$ directions are nearly the same, whereas they differ from the dispersions along the $\Gamma-A$ direction.

As can be seen from the masses for the *wz* polytypes given in Table VI, the overall agreement (especially for the hh VB as well as the CB) with other calculations[13,86,90] for AlN and GaN (see Table VI) is much better than in the *zb* case. This also holds for the comparison with masses derived from measurements for *wz*-GaN.[93,94] It has to be pointed out again that due to the non-parabolicity especially of the lh band its mass in the plane perpendicular to the *c*-axis is sensitive to the **k** region chosen for its calculation. Consequently, if larger **k** regions play a role in the measurement, an increase of the lh mass is expected (cf. Fig. 4b).

As shown for GaN and InN in Fig. 5 the averages of the lh and ch in-plane masses are influenced by the spin-orbit splitting of the corresponding VBs. For example the two lh masses are 0.44 and 0.24 m_0 for GaN or 0.15 and 0.06 m_0 for InN instead of 0.31 m_0 or 0.09 m_0 in Table VI. Furthermore, the in-plane hole masses calculated in this work for *wz*-InN are much smaller than previous predictions.[85,92,95] This is traced back to the more accurate band-structure calculations with respect to the gap value and the inclusion of SOC.

It is observed that the effective masses decrease along the row *wz*-AlN, *wz*-GaN, and *wz*-InN (cf. Table VI). For the electron masses this tendency can be explained again by the coupling of *s*- and *p*-states, $E_{p\perp/\parallel}$, and the gaps, E_g or $E_g+\Delta_{cr}$. Using the estimates $m_{e\parallel}(\Gamma)/m_0 = 1/[1+E_{p\parallel}/E_g+\Delta_{cr}]$ and $m_{e\perp}(\Gamma)/m_0 = 1/[1+E_{p\perp}/E_g]$[60] one finds $m_{e\parallel}(\Gamma)/m_0 = 0.28$, 0.20, and 0.06 and $m_{e\perp}(\Gamma)/m_0 = 0.29$, 0.22, and 0.06 based on the computed energy values. Indeed, these estimated values are not too far from the results of the full calculations in Table VI and, hence, explain the chemical trend and the symmetry-induced mass splitting.

V. SUMMARY AND CONCLUSIONS

In this paper the ground-state (energetic, structural, elastic) and excited-state (energy bands and band parameters) properties of the *zb* and the *wz* polytypes of AlN, GaN, and InN have been investigated using modern parameter-free approaches. From the comparison of different approximations of XC it has been shown that the AM05 XC functional gives rise to atomic geometries in excellent agreement with experimental data and, therefore, circumvents the overbinding (underbinding) of the LDA (PBE-GGA). Since the atomic positions are an important prerequisite for calculating the excited-state properties, the second part of the paper is based on the AM05 geometry results.

The electronic structure has been calculated by solving a QP equation which includes the XC self-energy of the electrons and holes within the G_0W_0 approximation, based on HSE eigenvalues and wave functions. The resulting gaps are in excellent agreement with experimental values. The influence of hydrostatic strain has been studied. Especially the fundamental energy gap of InN varies dramatically with the strain as indicated by the large volume deformation potential.

It has been found that the influence of the relative QP corrections to the HSE eigenvalues on the VBs around Γ is small. The inclusion of the spin-orbit interaction into the HSE calculations allowed us to study the corresponding energy splittings and to determine $\mathbf{k}\cdot\mathbf{p}$ parameters. Thereby, the validity of the quasicubic approximation for *wz*-GaN and *wz*-InN has been found to be questionable, especially due to the influence of the semicore *d* electrons.

In addition, the effective electron and hole masses are calculated. In the case of the VBs (especially for *wz* polytypes) band crossings render a parabolic description unfeasible for too large **k** regions. Treating XC within the HSE approach, tends to increase the masses and, hence, to lower the band dispersion near Γ. We demonstrate the importance of the spin-orbit interaction for the dispersion and the splittings of the bands around the BZ center and, hence, for the exact band masses. The comparison

with measured effective masses shows good agreement with the computed values especially for GaN. For InN polytypes trustable effective masses have been derived.

ACKNOWLEDGMENTS

We thank F. Fuchs, R. Goldhahn, and P. Vogl for scientific discussions. The research presented here has been funded by the European Community within the ITN RAINBOW (GA No. 2008-2133238) within the Seventh Framework Programme (FP7/2007-2013) under grant agreement No. 211956, as well as by the Deutsche Forschungsgemeinschaft (Project No. Be1346/20-1). A. S. acknowledges the support of the Carl-Zeiss Stiftung. Part of this work was performed under the auspices of the U.S. Department of Energy at Lawrence Livermore National Laboratory under Contract DE-AC52-07A27344.

* E-mail: luiz-claudio.de-carvalho@uni-jena.de

1 I. Vurgaftman and J. R. Meyer, J. Appl. Phys. **94**, 3675 (2003).
2 J. Wu, W. Walukiewicz, W. Shan, K. M. Yu, J. W. A. III, S. X. Li, E. E. Haller, H. Lu, and W. J. Schaff, J. Appl. Phys. **94**, 4457 (2003).
3 I. Gherasoiu, M. O'Steen, T. Bird, D. Gotthold, A. Chandolu, D. Y. Song, S. X. Xu, M. Holtz, S. A. Nikishin, and W. J. Schaff, Phys. Status Solidi C **5**, 1642 (2008).
4 V. Davydov, A. Klochikhin, V. Emtsev, D. Kurdyukov, S. Ivanov, V. Vekshin, F. Bechstedt, J. Furthmüller, J. Aderhold, J. Graul, A. Mudryi, H. Harima, A. Hashimoto, A. Yamamoto, and E. E. Haller, Phys. Status Solidi B **234**, 787 (2002).
5 T. L. Tansley and R. J. Egan, Phys. Rev. B **45**, 10942 (1992).
6 J. Wu, J. Appl. Phys. **106**, 011101 (2009).
7 T. Fehlberg, C. Gallinat, G. Umana-Membreno, G. Koblmüller, B. Nener, J. Speck, and G. Parish, J. Electron. Mater. **37**, 593 (2008).
8 S. Nakamura, Science **281**, 956 (1998).
9 E. Kioupakis, P. Rinke, A. Schleife, F. Bechstedt, and C. G. Van de Walle, Phys. Rev. B **81**, 241201 (2010).
10 H. Lu, W. J. Schaff, and L. F. Eastman, J. Appl. Phys. **96**, 3577 (2004).
11 S. Kako, C. Santori, K. Hoshino, S. Gotzinger, Y. Yamamoto, and Y. Arakawa, Nature Materials **5**, 887 (2006).
12 D. J. As, D. Schikora, and K. Lischka, Phys. Status Solidi C **0**, 1607 (2003).
13 P. Rinke, M. Winkelnkemper, A. Qteish, D. Bimberg, J. Neugebauer, and M. Scheffler, Phys. Rev. B **77**, 075202 (2008).
14 A. Svane, N. E. Christensen, I. Gorczyca, M. van Schilfgaarde, A. N. Chantis, and T. Kotani, Phys. Rev. B **82**, 115102 (2010).
15 A. Schleife, C. Rödl, F. Fuchs, J. Furthmüller, and F. Bechstedt, Appl. Phys. Lett. **91**, 241915 (2007).
16 A. Schleife, C. Rödl, F. Fuchs, J. Furthmüller, F. Bechstedt, P. H. Jefferson, T. D. Veal, C. F. McConville, L. F. J. Piper, A. DeMasi, K. E. Smith, H. Lösch, R. Goldhahn, C. Cobet, J. Zúñiga-Pérez, and V. Muñoz-Sanjosé, J. Korean Phys. Soc. **53**, 2811 (2008).
17 A. Schleife, F. Fuchs, C. Rödl, J. Furthmüller, and F. Bechstedt, Phys. Status Solidi B **246**, 2150 (2009).
18 A. Schleife, J. B. Varley, F. Fuchs, C. Rödl, F. Bechstedt, P. Rinke, A. Janotti, and C. G. Van de Walle, Phys. Rev. B **83**, 035116 (2011).
19 P. Hohenberg and W. Kohn, Phys. Rev. **136**, B864 (1964).
20 W. Kohn and L. J. Sham, Phys. Rev. **140**, A1133 (1965).
21 R. Armiento and A. E. Mattsson, Phys. Rev. B **72**, 085108 (2005).
22 R. Armiento and A. E. Mattsson, Phys. Rev. B **66**, 165117 (2002).
23 A. E. Mattsson, R. Armiento, J. Paier, G. Kresse, J. M. Wills, and T. R. Mattsson, J. Chem. Phys. **128**, 084714 (2008).
24 F. D. Murnaghan, P. Nat. Acad. Sci. USA **30**, 244 (1944), `http://www.pnas.org/content/30/9/244.short`.
25 J. P. Perdew and A. Zunger, Phys. Rev. B **23**, 5048 (5 1981).
26 J. P. Perdew, K. Burke, and M. Ernzerhof, Phys. Rev. Lett. **77**, 3865 (1996).
27 G. Kresse and J. Furthmüller, Comp. Mater. Sci. **6**, 15 (1996).
28 G. Kresse and D. Joubert, Phys. Rev. B **59**, 1758 (1 1999).
29 P. E. Blöchl, Phys. Rev. B **50**, 17953 (1994).
30 H. J. Monkhorst and J. D. Pack, Phys. Rev. B **13**, 5188 (1976).
31 W. G. Aulbur, L. Jönsson, and J. W. Wilkins, in *Advances in Research and Applications*, Solid State Physics, Vol. 54, edited by H. Ehrenreich and F. Spaepen (Academic Press, 1999) pp. 1–218.
32 G. Onida, L. Reining, and A. Rubio, Rev. Mod. Phys. **74**, 601 (2002).
33 L. Hedin, Phys. Rev. **139**, A796 (1965).
34 L. Hedin and S. Lundqvist, in *Advances in Research and Applications*, Solid State Physics, Vol. 23, edited by D. T. Frederick Seiz and H. Ehrenreich (Academic Press, 1970) pp. 1–181.
35 S. V. Faleev, M. van Schilfgaarde, and T. Kotani, Phys. Rev. Lett. **93**, 126406 (2004).
36 M. Shishkin and G. Kresse, Phys. Rev. B **75**, 235102 (2007).
37 F. Fuchs, J. Furthmüller, F. Bechstedt, M. Shishkin, and G. Kresse, Phys. Rev. B **76**, 115109 (2007).
38 M. van Schilfgaarde, T. Kotani, and S. Faleev, Phys. Rev. Lett. **96**, 226402 (6 2006).
39 P. Rinke, A. Qteish, J. Neugebauer, C. Freysoldt, and M. Scheffler, New J. Phys. **7**, 126 (2005).
40 F. Bechstedt, F. Fuchs, and G. Kresse, Phys. Status Solidi B **246**, 1877 (2009).
41 A. V. Krukau, O. A. Vydrov, A. F. Izmaylov, and G. E. Scuseria, J. Chem. Phys. **125**, 224106 (2006).
42 J. Paier, M. Marsman, K. Hummer, G. Kresse, I. C. Gerber, and J. G. Ángyán, J. Chem. Phys. **124**, 154709 (2006).
43 J. Heyd, G. E. Scuseria, and M. Ernzerhof, J. Chem. Phys. **124**, 219906 (2006).
44 J. Paier, M. Marsman, K. Hummer, G. Kresse, I. C. Gerber, and J. G. Ángyán, J. Chem. Phys. **125**, 249901 (2006).
45 L. C. de Carvalho, A. Schleife, F. Fuchs, and F. Bechstedt, Appl. Phys. Lett. **97**, 232101 (2010).
46 D. Hobbs, G. Kresse, and J. Hafner, Phys. Rev. B **62**, 11556 (2000).
47 C. Rödl, F. Fuchs, J. Furthmüller, and F. Bechstedt, Phys. Rev. B **77**, 184408 (2008).
48 J. Heyd and G. E. Scuseria, J. Chem. Phys. **121**, 1187 (2004).
49 Properties of Group III Nitrides, in *EMIS Datareviews Series*, IEE INSPEC, Vol. 11, edited by J. H. Edgar (1994).
50 M. E. Sherwin and T. J. Drummond, J. Appl. Phys. **69**, 8423 (1991).
51 H. Landolt and R. Börnstein, *Numerical Data and Functional Relationships in Science and Technology*, Vol. III, No. 17a and 22a (Springer-Verlag, Berlin, 1982).
52 Q. Xia, H. Xia, and A. L. Ruoff, J. Appl. Phys. **73**, 8198 (1993).
53 H. Schulz and K. H. Thiemann, Solid State Commun. **23**, 815 (1977).
54 M. Ueno, M. Yoshida, A. Onodera, O. Shimomura, and K. Takemura, Phys. Rev. B **49**, 14 (1994).

[55] A. García and M. L. Cohen, Phys. Rev. B **47**, 4215 (1993).
[56] C.-Y. Yeh, Z. W. Lu, S. Froyen, and A. Zunger, Phys. Rev. B **46**, 10086 (1992).
[57] Sargent-Welch, Table of Periodic Properties of Elements(1980).
[58] F. Bechstedt, F. Fuchs, and J. Furthmüller, Phys. Status Solidi A **207**, 1041 (2010).
[59] A. Riefer, F. Fuchs, C. Rödl, A. Schleife, F. Bechstedt, and Goldhahn, Phys. Rev. B **84**, in press (2011).
[60] P. Y. Yu and M. Cardona, *Fundamentals of Semiconductors: Physics and Material Properties* (Springer, 1995).
[61] L. P. Bouckaert, R. Smoluchowski, and E. Wigner, Phys. Rev. **50**, 58 (Jul 1936).
[62] E. I. Rashba, Fiz. Tverd. Tela **1**, 407 (1959).
[63] F. Bechstedt, in *Low-Dimensional Nitride Semiconductors* (Oxford University Press, 2002) Chap. Nitrides as seen by a theorist.
[64] W. Harrison, *Electronic Structure and the Properties of Solids* (Dover Pub., New York, 1989).
[65] S.-H. Wei and A. Zunger, Phys. Rev. B **37**, 8958 (1988).
[66] C. Persson and A. Zunger, Phys. Rev. B **68**, 073205 (2003).
[67] P. D. C. King, T. D. Veal, C. F. McConville, F. Fuchs, J. Furthmüller, F. Bechstedt, J. Schörmann, D. J. As, K. Lischka, H. Lu, and W. J. Schaff, Phys. Rev. B **77**, 115213 (3 2008).
[68] M. Röppischer, R. Goldhahn, G. Rossbach, P. Schley, C. Cobet, N. Esser, T. Schupp, K. Lischka, and D. J. As, J. Appl. Phys. **106**, 076104 (2009).
[69] J. Schörmann, D. J. As, K. Lischka, P. Schley, R. Goldhahn, S. F. Li, W. Löffler, M. Hetterich, and H. Kalt, Appl. Phys. Lett. **89**, 261903 (2006).
[70] F. Litimein, B. Bouhafs, G. Nouet, and P. Ruterana, phys. stat. sol. (b) **243**, 1577 (2006).
[71] J. Furthmüller, P. H. Hahn, F. Fuchs, and F. Bechstedt, Phys. Rev. B **72**, 205106 (11 2005).
[72] M. Cardona and N. E. Christensen, Solid State Commun. **116**, 421 (2000).
[73] J. P. Desclaux, Atom. Data Nucl. Data **12**, 311 (1973).
[74] M. Cardona, N. E. Christensen, and G. Fasol, Phys. Rev. B **38**, 1806 (1988).
[75] S. L. Chuang and C. S. Chang, Phys. Rev. B **54**, 2491 (1996).
[76] G. Dresselhaus, Phys. Rev. **100**, 580 (1955).
[77] M. Cardona, N. E. Christensen, and G. Fasol, Phys. Rev. Lett. **56**, 2831 (1986).
[78] M. P. Surh, M.-F. Li, and S. G. Louie, Phys. Rev. B **43**, 4286 (1991).
[79] L. C. Lew Yan Voon, M. Willatzen, M. Cardona, and N. E. Christensen, Phys. Rev. B **53**, 10703 (1996).
[80] J. Wu, W. Walukiewicz, W. Shan, K. M. Yu, J. W. Ager, E. E. Haller, H. Lu, and W. J. Schaff, Phys. Rev. B **66**, 201403 (2002).
[81] S. P. Fu and Y. F. Chen, Appl. Phys. Lett. **85**, 1523 (2004).
[82] A. V. Rodina and B. K. Meyer, Phys. Rev. B **64**, 245209 (2001).
[83] S. Shokhovets, G. Gobsch, and O. Ambacher, Appl. Phys. Lett. **86**, 161908 (2005).
[84] L. E. Ramos, L. K. Teles, L. M. R. Scolfaro, J. L. P. Castineira, A. L. Rosa, and J. R. Leite, Phys. Rev. B **63**, 165210 (2001).
[85] D. Fritsch, H. Schmidt, and M. Grundmann, Phys. Rev. B **67**, 235205 (2003).
[86] K. Kim, W. R. L. Lambrecht, B. Segall, and M. van Schilfgaarde, Phys. Rev. B **56**, 7363 (1997).
[87] D. Fritsch, H. Schmidt, and M. Grundmann, Phys. Rev. B **69**, 165204 (2004).
[88] M. Fanciulli, T. Lei, and T. D. Moustakas, Phys. Rev. B **48**, 15144 (1993).
[89] P. Schley, C. Napierala, R. Goldhahn, G. Gobsch, J. Schörmann, D. J. As, K. Lischka, M. Feneberg, K. Thonke, F. Fuchs, and F. Bechstedt, Phys. Status Solidi C **5**, 2342 (2008).
[90] M. Suzuki, T. Uenoyama, and A. Yanase, Phys. Rev. B **52**, 8132 (1995).
[91] M. Goano, E. Bellotti, E. Ghillino, G. Ghione, and K. F. Brennan, J. Appl. Phys. **88**, 6467 (2000).
[92] Y. C. Yeo, T. C. Chong, and M. F. Li, J. Appl. Phys. **83**, 1429 (1998).
[93] J. S. Im, A. Moritz, F. Steuber, V. Härle, F. Scholz, and A. Hangleiter, Appl. Phys. Lett. **70**, 631 (1997).
[94] M. Steube, K. Reimann, D. Fröhlich, and S. J. Clarke, Appl. Phys. Lett. **71**, 948 (1997).
[95] B. Rezaei, A. Asgari, and M. Kalafi, Physica B **371**, 107 (2006).
[96] M. Goiran, M. Millot, J.-M. Poumirol, I. Gherasoiu, W. Walukiewicz, and J. Leotin, Appl. Phys. Lett. **96**, 052117 (2010).

FIGURES

Figure 1. QP band structures and DOS without spin-orbit interaction for *zb*-AlN, *zb*-GaN, and *zb*-InN. The numbers indicate the irreducible representations at the respective high-symmetry points using the notation according to Bouckaert, Smoluchowski and Wigner (see Ref. 60). The Γ_{15} VB maximum is used as energy zero. The fundamental band gap is indicated by the shaded region.

Figure 2. QP band structures and DOS without spin-orbit interaction for *wz*-AlN, *wz*-GaN, and *wz*-InN. The numbers indicate the irreducible representations at the respective high-symmetry points using the Rashba notation (see Ref. 62). The Γ_6 (GaN, InN) or Γ_1 (AlN) VB maximum is used as energy zero. The fundamental band gap is indicated by the shaded region.

Figure 3. (Color online) Geometric solution of Eq. (1) to relate the $\Delta E_{1/2}$ values (cf. Table IV) and $\Delta_{\rm cf}$, $\Delta_{\rm so\|}$, and $\Delta_{\rm so\perp}$ for *wz*-GaN. The black line represents $\Delta_{\rm so\|}$ while the blue ellipsoid gives $\Delta_{\rm so\perp}$. The two crossings indicate the two possible solutions within the quasicubic approximation.

Figure 4. The HSE+SOC results for the uppermost VBs of AlN, GaN, and InN in (a) the *zb* and (b) the *wz* structure are shown along two high-symmetry directions in the BZ. Up to $1/16$ of the paths $\Gamma-X$, $\Gamma-L$, and $\Gamma-M$ in the BZ is shown, as well as $1/12$ of the $\Gamma-A$ path. The heavy-hole (hh), light-hole (lh), spin-orbit split-off (so), and crystal-field split-off (ch) bands are labeled and the top of the VBs is used as energy zero.

Figure 5. (Color online) The spin-orbit-induced splittings for the *wz* nitrides in the proximity of Γ are shown along the $\Gamma-M$ direction. The hh (red open circles), the lh (blue triangles), and the ch (green squares) bands are given. For comparison the splittings for the lowest CB (black circles) are included.

TABLES

Table I. The cubic lattice constant a_0 (in Å) and the hexagonal lattice parameters a, c (in Å) as well as c/a and the internal parameter u are given for AlN, GaN and InN polytypes. The volume per cation-anion pair $\Omega_{\rm pair}$ (in Å^3) is also listed. In addition, also the bulk moduli B_0 (in GPa) and their derivatives with respect to pressure B_0' as derived from fits to the Murnaghan equation of state are given. The difference of the total energies $\Delta E_{\rm tot}$ in (meV/pair) between the *zb* and the *wz* polymorphs is included. Results are derived from calculations using the LDA, PBE-GGA, and AM05 XC functionals and, for comparison, experimental values are listed.

		AM05	LDA	PBE-GGA	Expt.
zb-AlN	a_0	4.374	4.343	4.402	4.37[a]
	$\Omega_{\rm pair}$	20.922	20.482	21.328	
	B_0	204.7	212.0	193.2	202[b]
	B_0'	4.38	3.22	4.16	
	$\Delta E_{\rm tot}$	47	46	41	
zb-GaN	a_0	4.495	4.465	4.547	4.49[c]
	$\Omega_{\rm pair}$	22.710	22.257	23.509	
	B_0	181.9	188.8	172.0	190[b]
	B_0'	4.07	4.44	3.36	
	$\Delta E_{\rm tot}$	15	14	18	
zb-InN	a_0	5.005	4.959	5.059	4.98[a]
	$\Omega_{\rm pair}$	31.346	30.493	32.371	
	B_0	130.8	144.7	120.2	136[b]
	B_0'	4.07	4.95	4.10	
	$\Delta E_{\rm tot}$	24	24	70	
wz-AlN	a	3.112	3.088	3.129	3.11[e]
	c	4.976	4.946	5.018	4.978[e]
	c/a	1.599	1.601	1.603	1.601[e]
	u	0.380	0.379	0.379	0.382[e]
	$\Omega_{\rm pair}$	20.869	20.420	21.276	
	B_0	202.3	210.8	187.2	185[d]
	B_0'	4.36	3.95	4.02	5.7[d]
wz-GaN	a	3.181	3.158	3.217	3.19[e]
	c	5.180	5.145	5.241	5.166 – 5.185[e]
	c/a	1.628	1.629	1.629	1.627[e]

	u	0.376	0.376	0.376	0.377[e]
	Ω_{pair}	22.698	22.219	23.488	
	B_0	183.2	197.4	172.2	188[d]
	B_0'	4.17	4.23	4.63	4.3[f]
wz-InN	a	3.549	3.517	3.587	3.54[f]
	c	5.736	5.685	5.789	5.718[e]
	c/a	1.616	1.616	1.613	1.613[f]
	u	0.378	0.377	0.378	0.375[b]
	Ω_{pair}	31.293	30.451	32.253	
	B_0	131.3	145.3	120.9	125.5[f]
	B_0'	4.76	4.52	5.37	12.7[f]

[a] Collection of experimental data in Ref. 49
[b] Ref. 50 - Force balance method.
[c] Collection of experimental data in Ref. 51
[d] Ref. 52 - X-ray diffraction.
[e] Ref. 53 - X-ray diffraction.
[f] Ref. 54 - X-ray diffraction.

Table II. Energies E_g (in eV) of the fundamental band gaps at Γ obtained within HSE+G_0W_0. For the AM05 equilibrium geometry, the hydrostatic pressure coefficients α_P (in meV/GPa) and the volume deformation potentials α_V (in eV) of the fundamental band gap are given. In the case of *zb*-AlN the values in parenthesis refer to the indirect gap between Γ and X.

		geometry: AM05	geometry: LDA	geometry: PBE-GGA	Expt.
zb-AlN	E_g	6.271	6.659	6.071	5.93[a]
		(5.198)	(5.265)	(5.164)	(5.3)[a]
	α_V	-10.11			
		(-2.40)			
	α_P	49.4			
		(11.7)			
zb-GaN	E_g	3.427	3.609	3.158	3.3[b]
	α_V	-8.60			-7.9[b]
	α_P	47.3			40 – 46[b]
zb-InN	E_g	0.414	0.540	0.264	0.61[c]
	α_V	-4.48			
	α_P	34.2			31[b]
wz-AlN	E_g	6.310	6.553	6.144	6.28[d]
	α_V	-10.07			
	α_P	49.8			49[b]
wz-GaN	E_g	3.659	3.847	3.366	3.51[d]
	α_V	-8.52			
	α_P	46.5			37 – 47[b]
wz-InN	E_g	0.638	0.765	0.494	0.7[d,e]
	α_V	-4.56			
	α_P	34.7			22 – 30[b]

[a] Ref. 68 - Spectroscopic ellipsometry.
[b] Collection of experimental data in Ref. 51
[c] Ref. 69 - Photoluminescence.
[d] Collection of experimental data in Ref. 70
[e] Ref. 2 - Photoluminescence.

Table III. Fundamental band gaps E_g (in eV) of *zb*-AlN, *zb*-GaN, and *zb*-InN calculated for the LDA, PBE-GGA, and the AM05 equilibrium geometries. Three different approximations for the XC self-energy are compared: (i) "(semi-)local" means that the same XC functional as for the calculation of the atomic geometry has been used. In addition, the gaps calculated using (ii) the HSE functional, and (iii) the HSE+G_0W_0 approach are included.

	XC self-energy	AM05	LDA	PBE-GGA
zb-AlN	(semi-)local	3.198	2.977	3.312
	HSE	4.333	4.354	4.316
	HSE+G_0W_0	5.198	5.265	5.164
zb-GaN	(semi-)local	1.843	1.925	1.572
	HSE	2.844	2.972	2.590
	HSE+G_0W_0	3.427	3.609	3.158
zb-InN	(semi-)local	≈ 0.0	≈ 0.0	≈ 0.0
	HSE	0.325	0.416	0.206
	HSE+G_0W_0	0.414	0.540	0.264

Table IV. Different energy splittings (from HSE calculations) of the uppermost VB states of the nitrides in three different equilibrium geometries are given in meV: The spin-orbit splitting constants at the BZ center Γ, $\Delta_{so} = \varepsilon(\Gamma_{8v}) - \varepsilon(\Gamma_{6v})$, and at the L point, $\Delta_{so}(L) = \varepsilon(L_{4,5}) - \varepsilon(L_6)$, for *zb* polymorphs as well as $\Delta E_1 = \varepsilon(\Gamma_{9v}) - \varepsilon(\Gamma_{7+v})$ and $\Delta E_2 = \varepsilon(\Gamma_{9v}) - \varepsilon(\Gamma_{7-v})$ for *wz* polymorphs are calculated from the HSE eigenvalues including SOC. The crystal-field splittings $\Delta^0_{cf} = \varepsilon(\Gamma_5) - \varepsilon(\Gamma_1)$ (in the absence of SOC) are also given. The values Δ^{qc}_{cf} are derived within the quasicubic approximation. The spin-orbit interaction constants $\Delta_{so\parallel}$ as well as $\Delta_{so\perp}$ are derived using Δ^0_{cf} for the crystal-field splitting (see text). The respective HSE+G_0W_0 results are provided in parenthesis.

		AM05	LDA	PBE-GGA	Expt.
zb-AlN	$\Delta_{so}(\Gamma)$	21.8	21.9	21.8	19[a]
	$\Delta_{so}(L)$	16.9	17.0	16.8	
zb-GaN	$\Delta_{so}(\Gamma)$	20.2	19.4	21.6	17[a]
	$\Delta_{so}(L)$	31.3	31.2	31.6	
zb-InN	$\Delta_{so}(\Gamma)$	17.4	14.4	20.7	5[a]
	$\Delta_{so}(L)$	53.7	53.0	54.3	
wz-AlN	Δ^0_{cf}	−257.2	−242.7	−217.2	−169[b]
		(−275.7)	(−260.0)	(−234.3)	
	ΔE_1	−250.4	−235.9	−210.5	
		(−268.9)	(−253.2)	(−227.6)	
	ΔE_2	14.9 (14.9)	14.9 (14.9)	14.9 (14.9)	
	Δ^{qc}_{cf}	−257.3	−242.7	−217.3	−230[b]
		(−275.8)	(−260.1)	(−234.4)	
	Δ^{qc}_{so}	21.8 (21.8)	21.7 (21.8)	21.7 (21.7)	19[b]
	$\Delta_{so\parallel}$	21.7 (21.7)	21.7 (21.7)	21.6 (21.6)	
	$\Delta_{so\perp}$	22.7 (23.5)	22.1 (22.8)	22.5 (23.3)	
wz-GaN	Δ^0_{cf}	32.2 (26.4)	40.9 (34.5)	32.0 (27.3)	10[b]
	ΔE_1	8.4 (8.4)	8.7 (8.7)	9.0 (9.0)	
	ΔE_2	41.8 (36.0)	49.3 (42.9)	42.6 (37.9)	
	Δ^{qc}_{cf}	35.3 (28.5)	43.1 (36.1)	35.3 (29.6)	39[b]
	Δ^{qc}_{so}	14.9 (15.9)	14.9 (15.5)	16.3 (17.3)	17[b], 8[b]
	$\Delta_{so\parallel}$	18.0 (18.0)	17.1 (17.1)	19.6 (19.6)	
	$\Delta_{so\perp}$	22.0 (19.7)	21.5 (19.6)	23.2 (21.3)	
wz-InN	Δ^0_{cf}	34.6 (31.7)	41.3 (38.5)	25.1 (22.1)	40[b]
	ΔE_1	6.3 (6.3)	5.4 (5.4)	6.3 (6.3)	
	ΔE_2	42.8 (39.9)	47.4 (44.7)	36.5 (33.5)	
	Δ^{qc}_{cf}	38.6 (35.6)	44.1 (41.3)	32.0 (28.8)	39[b]
	Δ^{qc}_{so}	10.5 (10.6)	8.7 (8.8)	10.8 (11.0)	5[b]
	$\Delta_{so\parallel}$	14.5 (14.5)	11.5 (11.6)	17.7 (17.7)	
	$\Delta_{so\perp}$	22.4 (21.4)	20.1 (19.7)	24.7 (23.2)	

[a] Collection of experimental data in Ref. 49
[b] Collection of experimental data in Ref. 51

Table V. Effective heavy-hole (hh), light-hole (lh), spin-orbit split-off hole (so), and electron (e) masses (in units of the free-electron mass m_0) as derived from the HSE band structure (including SOC) of *zb*-AlN, *zb*-GaN and *zb*-InN. While hh and lh masses along the [100], [110], and [111] directions are given, only the isotropic mass for the so case is included. The values for the hh and lh masses represent averages along $\Gamma - L$ and $\Gamma - K$. For AlN, longitudinal and transverse electron masses are included also for the X point. The results are compared with values from other calculations and experiment.

	$m_{hh}^{[100]}$	$m_{lh}^{[100]}$	$m_{hh}^{[110]}$	$m_{lh}^{[110]}$	$m_{hh}^{[111]}$	$m_{lh}^{[111]}$	m_{so}	$m_e(\Gamma)$
zb-AlN								
This work	1.32	0.44	2.32	0.39	3.98	0.38	0.55	0.30
[a]	1.44	0.42	3.03	0.37	4.24	0.36	0.63	0.28
[b]	1.02	0.37	1.89	0.32	2.64	0.30	0.54	0.23
[c]	1.33	0.47	2.63	0.40	3.91	0.38		0.32
[d]								0.33
zb-GaN								
This work	0.83	0.28	1.59	0.25	1.95	0.23	0.34	0.19
[a]	0.86	0.21	1.65	0.19	2.09	0.19	0.30	0.14
[b]	0.84	0.22	1.52	0.20	2.07	0.19	0.35	0.14
[c]	0.81	0.27	1.38	0.23	1.81	0.22		0.19
[d]								0.19
Expt.[f]								0.15
zb-InN								
This work	0.91	0.079	1.55	0.065	1.89	0.070	0.11	0.052

[c]	0.84	0.080	1.37	0.078	1.74	0.077		0.054
[e]	1.26	0.100	2.22	0.097	2.74	0.096	0.19	0.066
Expt.[g]								0.041

[a] Ref. 84 - DFT-LDA.
[b] Ref. 85 - Empirical pseudopotential method - Ionic model potential.
[c] Ref. 13 - DFT-OEPx + G_0W_0.
[d] Ref. 86 - LMTO-LDA.
[e] Ref. 87 - Empirical pseudopotential method - Ionic model potential.
[f] Ref. 88 - Electron spin resonance measurement.
[g] Ref. 89 - Spectroscopic ellipsometry.

Table VI. Effective heavy-hole (hh), light-hole (lh), crystal-field split-off hole (ch), and electron (e) masses (in units of the free-electron mass m_0) as derived from the HSE band structure including SOC of *wz*-AlN, *wz*-GaN and *wz*-InN. The masses are evaluated along the $\Gamma-A$, $\Gamma-M$, and $\Gamma-K$ direction in the BZ. The results are compared with values from other calculations and experiments.

	m^A_{hh}	m^A_{lh}	m^A_{ch}	m^A_e	$m^{M,K}_{hh}$	$m^{M,K}_{lh}$	$m^{M,K}_{ch}$	$m^{M,K}_e$
wz-AlN								
This work	3.31	3.06	0.26	0.32	6.95	0.35	3.47	0.34
[a]	2.37	2.37	0.21	0.23	3.06	0.29	1.20	0.24
[b]	3.68	3.68	0.25	0.33	6.33	0.25	3.68	0.25
[c]	3.53	3.53	0.26	0.35	11.14	0.33	4.05	0.35
[d]				0.29				0.34
Expt. [i]				0.29-0.45				0.29-0.45
wz-GaN								
This work	2.00	1.22	0.20	0.21	0.57	0.31	0.92	0.21
[c]	2.00	1.19	0.17	0.35	0.34	0.35	1.27	0.35
[e]	1.76	1.76	0.14	0.19	1.69	0.14	1.76	0.17
[f]	1.88	0.92	0.19	0.19	0.33	0.36	1.27	0.21
Expt.	2.20[g]	1.10[h]	0.30[i]	0.20[i]	0.42[i]	0.51[i]	0.68[i]	0.20[i]
wz-InN								
This work	1.98	1.02	0.08	0.06	0.44	0.09	0.18	0.06
[a]	2.44	2.44	0.14	0.14	2.66	0.15	3.42	0.14
[e]	1.56	1.56	0.10	0.11	1.68	0.11	1.39	0.10
[j]	1.39	1.39	0.10	0.12	1.41	0.12	1.69	0.11
Expt. [i]				0.07				0.07
[k]				0.055				0.055

[a] Ref. 85 - Empirical pseudopotential method - Ionic model potential.
[b] Ref. 90 - DFT-LDA.
[c] Ref. 86 - LMTO-LDA.
[d] Ref. 91 - Empirical pseudopotential method - Nonlocal pseudopotential.
[e] Ref. 92 - Empirical pseudopotential method - Form factors adjusted.
[f] Ref. 13 - DFT-OEPx + G_0W_0.
[g] Ref. 93 - Time-resolved photoluminescence.
[h] Ref. 94 - Two-photon spectroscopy.
[i] Collection of experimental data in Ref. 13
[j] Ref. 95 - Empirical pseudopotential method - Adjusted pseudopotential.
[k] Ref. 96 - Cyclotron effective mass measurement.

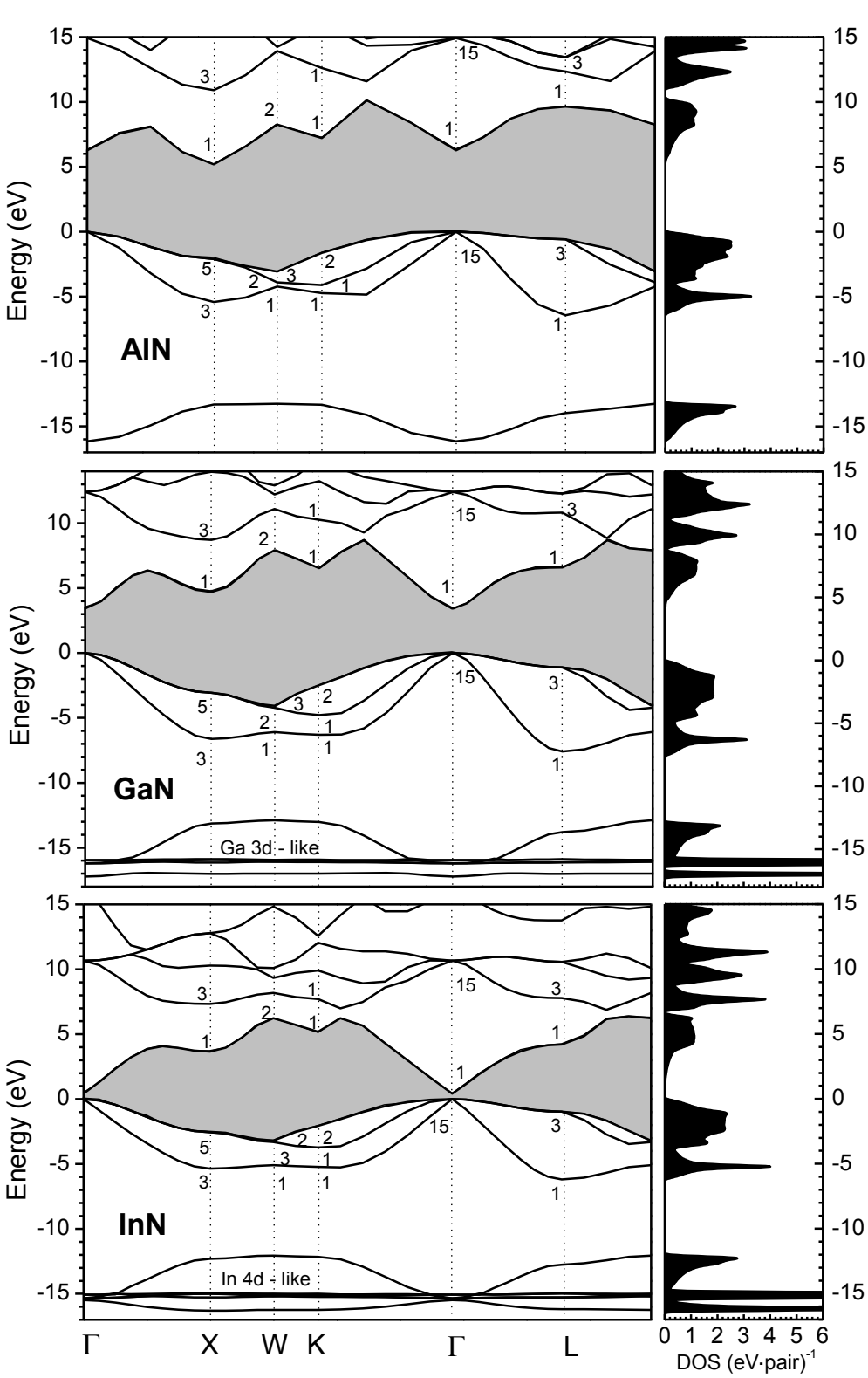
Energy (eV)
AlN
GaN
Ga 3d - like
InN
In 4d - like
Γ
X
W
K
Γ
L
DOS (eV·pair)$^{-1}$

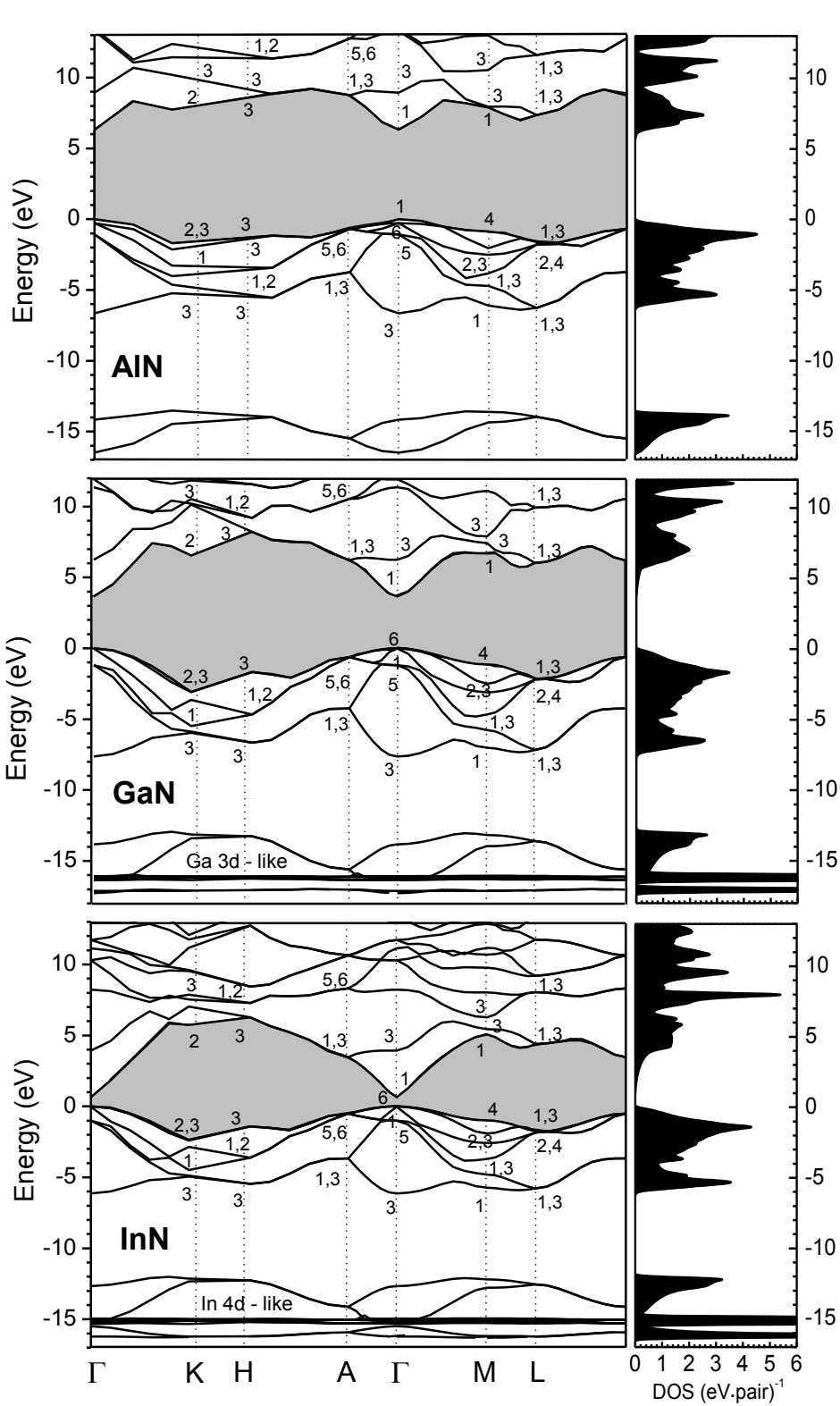
Energy (eV)
AlN
GaN
Ga 3d - like
InN
In 4d - like
Γ
K
H
A
Γ
M
L
DOS (eV·pair)$^{-1}$

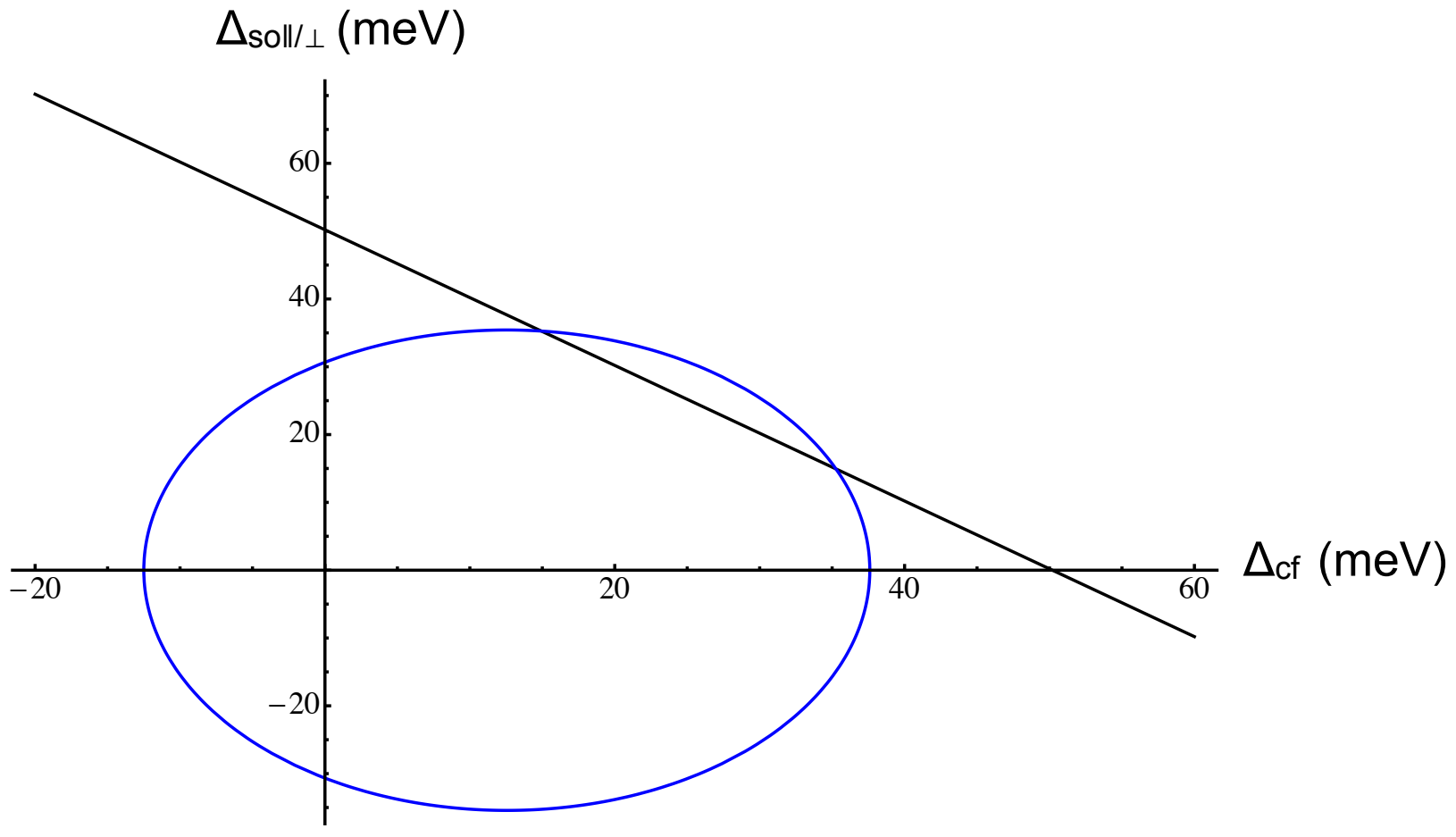
Δsoll/⊥ (meV)
60
40
20
−20
−20
20
40
60
Δcf (meV)

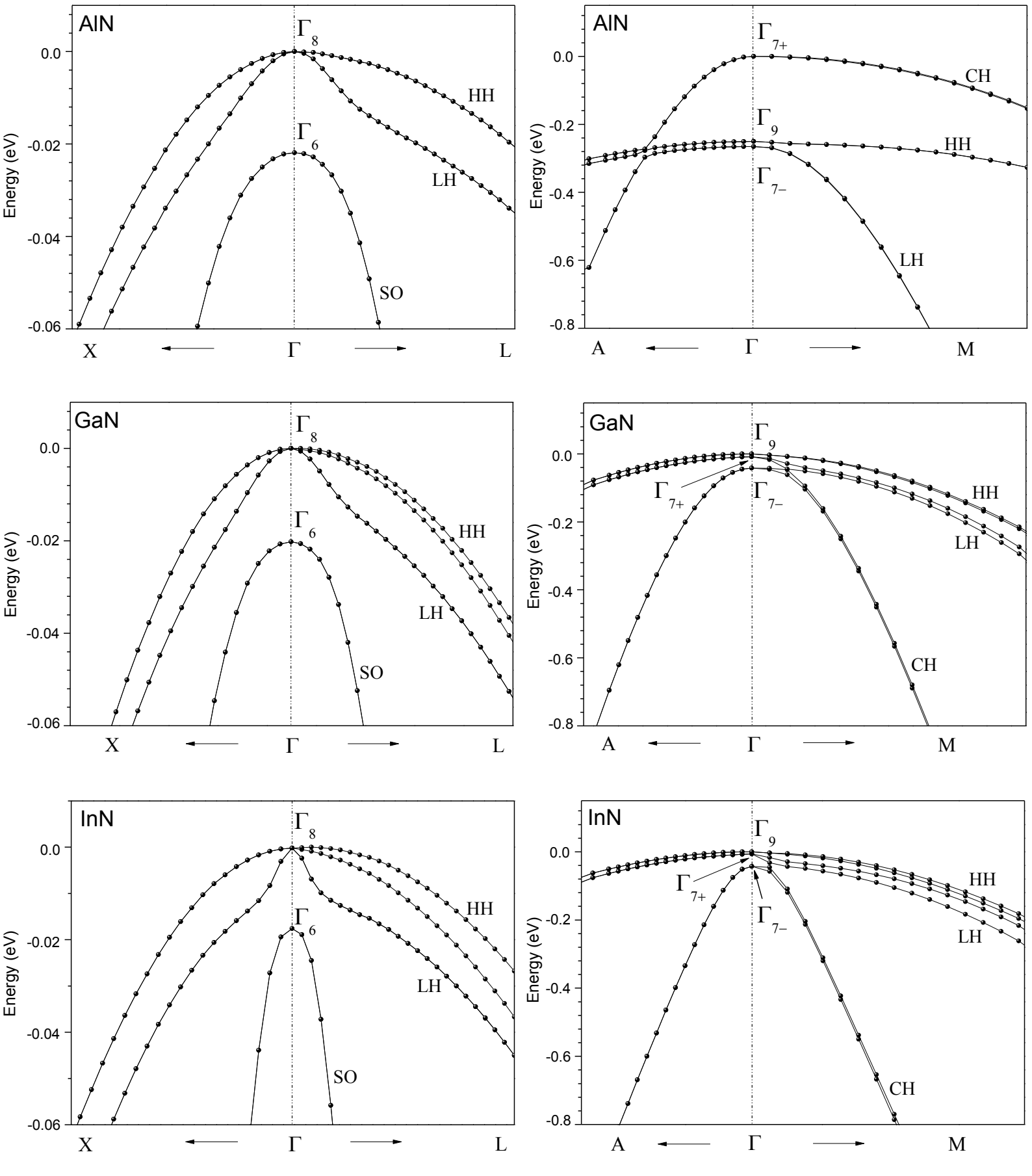
AlN
Γ8
Γ6
HH
LH
SO
Energy (eV)
0.0
-0.02
-0.04
-0.06
X
Γ
L
AlN
Γ7+
Γ9
Γ7−
CH
HH
LH
-0.2
-0.4
-0.6
-0.8
A
Γ
M
GaN
Γ8
Γ6
HH
LH
SO
Γ9
Γ7+
Γ7−
CH
InN
Γ8
Γ6
HH
LH
SO
Γ9
Γ7+
Γ7−
CH

(a) (b)

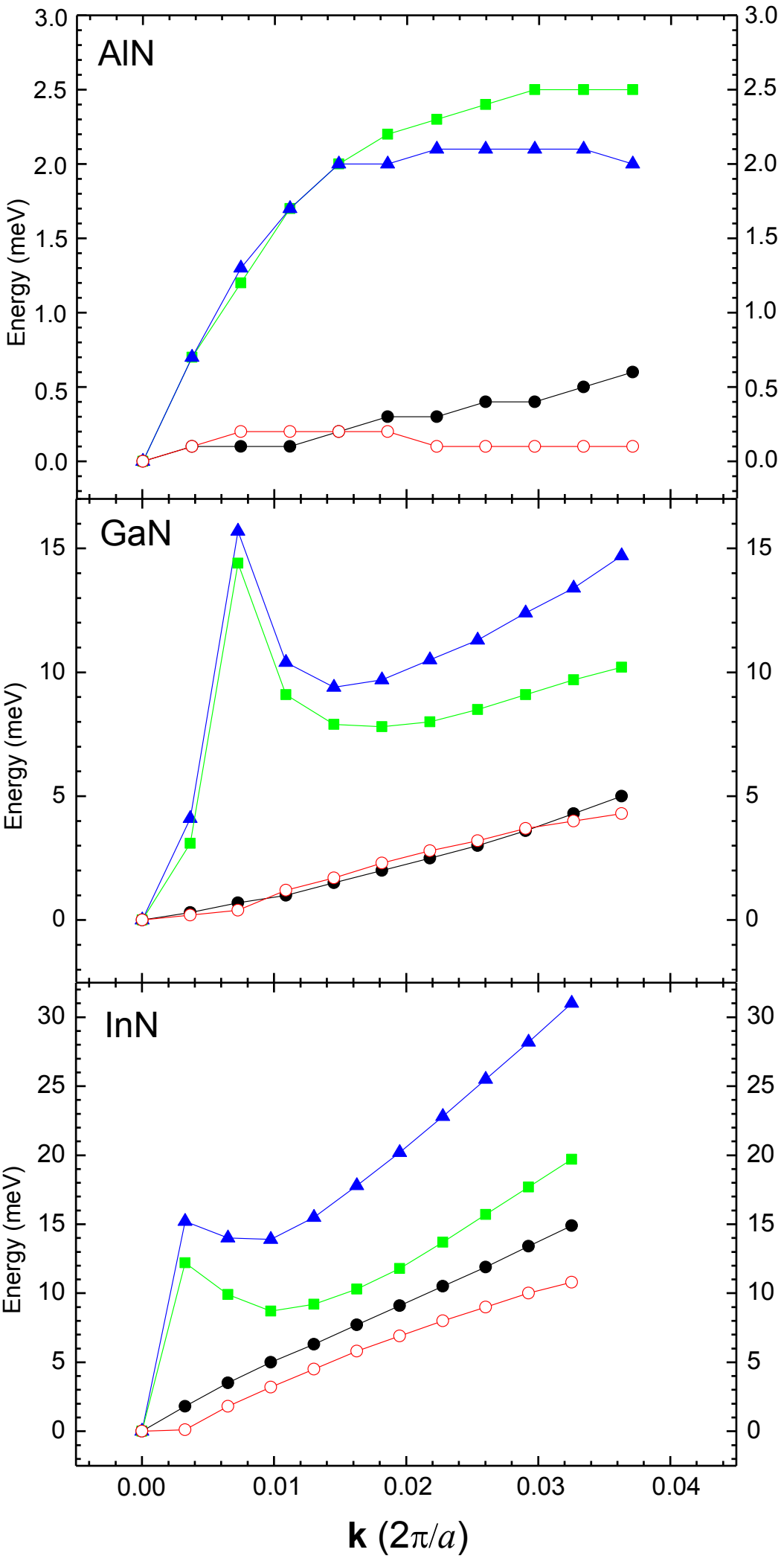
AlN
GaN
InN
Energy (meV)
Energy (meV)
Energy (meV)
3.0
2.5
2.0
1.5
1.0
0.5
0.0
15
10
5
0
30
25
20
15
10
5
0
0.00
0.01
0.02
0.03
0.04
k (2π/a)